Heliyon 11 (2025) e39913

Contents lists available at ScienceDirect

Heliyon

journal homepage: www.cell.com/heliyon

Research article

The stability improvements of dye-sensitized solar cell with natural template for photoanode using lignin extracted from rice husk

Gita Rabelsa [a,b], Shobih [b], Jojo Hidayat [b], Phutri Milana [b], Widhya Budiawan [b], Erdin Almuqqodas [a,b], Natalita M. Nursam [b], Ahmad Ibrahim [a,c], Lia M. Pranoto [a,b], Yuliar Firdaus [b,**], Brian Yuliarto [a,*]

[a] Advanced Functional Materials Research Group, Faculty of Industrial Technology, Institut Teknologi Bandung, Bandung, 40132, Indonesia
[b] Research Center for Electronics, National Research and Innovation Agency, Bandung, 40135, Indonesia
[c] Energy Research Institute @ NTU, Nanyang Technological University, Research Techno Plaza, 50 Nanyang Drive, 637553, Singapore

ARTICLE INFO

Keywords:
Rice husk
Lignin
TiO_2
DSSC
Stability

ABSTRACT

In response to escalating global concerns over environmental pollution, the development of green dye-sensitized solar cells (DSSCs) has emerged as a promising technology for solar energy conversion. This study harnesses the potential of rice husk, an abundant agricultural waste in Indonesia, by extracting lignin through a simple recycling method. Lignin acts as a natural, non-toxic dopant and template for TiO_2 composites, enhancing the stability of the photoanode in DSSCs. A TiO_2 photoanode modified with 5 % lignin achieved a power conversion efficiency (PCE) of 4.81 %. After a 90-day stability test, the TiO_2/lignin 5 % composite retained 78 % of its initial PCE, significantly outperforming pristine TiO_2 in terms of short-circuit current density (J_{SC}) and open-circuit voltage (V_{OC}). This improved stability is attributed to increased porosity, better lignin dispersion within the TiO_2 matrix, prevention of agglomeration, enhanced surface area for dye adsorption, and reduced electrolyte leakage. Furthermore, lignin's high thermal stability on the TiO_2 surface provides additional protection against dye degradation and electrolyte evaporation during repeated light exposure.

1. Introduction

The global energy crisis presents a critical challenge, requiring innovative and cost-effective solutions for energy production and storage. The growing consumption of fossil fuels not only accelerates global warming but also contributes to severe environmental pollution. To reduce our reliance on fossil fuels, significant efforts have been made to develop renewable energy sources as sustainable alternatives [1]. Among these, solar energy stands out as a promising option, leveraging the sun's abundant power to generate electricity. Solar panels are engineered to capture sunlight and convert it into electrical energy via the photoelectric effect, offering a cleaner and more sustainable approach to energy production [2].

Silicon-based solar technology remains the most established in manufacturing but is hindered by high costs due to expensive

* Corresponding author.
** Corresponding author.
E-mail addresses: 23322002@mahasiswa.itb.ac.id (G. Rabelsa), yuliar.firdaus@brin.go.id (Y. Firdaus), brian@tf.itb.ac.id (B. Yuliarto).

https://doi.org/10.1016/j.heliyon.2024.e39913
Received 22 July 2024; Received in revised form 27 October 2024; Accepted 28 October 2024
Available online 28 November 2024

materials and energy-intensive production processes [3]. Among various third-generation solar cell technologies, dye-sensitized solar cells (DSSCs) have received significant attention for their cost-effectiveness, ease of fabrication, and tunable optical features [2,4,5]. However, ongoing research is focused on overcoming challenges associated with DSSCs, such as the limited light absorption of wide-bandgap TiO_2-based photoanodes, photocatalytic instability especially under UV light, and thermal instability at elevated temperatures [6].

DSSCs primarily consist of a photoanode, dye sensitizers, a redox electrolyte, a counter electrode, and a conductive substrate [7]. The photoanode plays a crucial role in addressing various performance challenges in DSSC design. It typically requires a single layer of dye molecules adsorbed onto the surface of a semiconductor, which is responsible for light absorption in the device [2]. Nanostructured semiconductor photoanode are essential due to their large surface area, which facilitates large number of dye adsorption. Titanium dioxide (TiO_2), particularly in its anatase crystal form, is the most commonly used material for these mesoporous photoanodes. To achieve the necessary porosity, enhance electronic connectivity, and improve mechanical stability, mesoporous TiO_2 are annealed at high temperatures (400–500 °C) to remove organic additives [3]. Thus, the porosity and pore size of these films are critical. Doping TiO_2 can improve its properties by modifying trap states, adjusting band edge levels, increasing dye adsorption, and stabilizing the anatase phase [8]. Previous studies have explored a range of TiO_2-based composites, such as copper/nitrogen (Cu/N), copper/-sulfur (Cu/S), copper/graphene (CuTGR), and aluminum/nitrogen (Al/N), nickel oxide (NiO) [9–13]. Additionally, to achieve optimal performance, many studies recommend applying a $TiCl_4$ treatment. This treatment enhances the structural, optical, electrical, and charge transport properties of TiO_2 photoanodes, significantly improving their ability to capture and convert light energy in DSSCs [14].

Several researchers have doped photoanodes with cadmium telluride (CdTe), a material that can be categorized as potentially hazardous [15]. To address concerns about cost and safety, alternative natural dopants such as banana stem fibers, butterfly wings, and other carbon-based materials have been explored. These natural dopants offer a promising solution for improving DSSC performance while maintaining affordability and environmental safety [16–18].

The large volume of the biomass side products from rice production is one of potential materials as a natural doping. China produced more than 148 million tonnes of milled rice during the 2021 to 2022 crop year, exceeding all other countries in volume. In this crop year, India ranked second among the producers with more than 129 million metric tons of processed rice. As the third rank, Indonesia produced more than 34 million metric tons of milled rice, followed by several countries that have produced smaller milled rice [19]. As a consequence of this vast agricultural output, waste generation, including rice husks, acccounting for approximately 20 % of paddy mass, is increasing and often discarded unsustainably through open dumping or incineration [20]. Rice husk contains 31.13 % cellulose, 17.71 % hemicellulose, and 28.25 % lignin [21]. Globally, plants produce around 150 billion tons of lignin annually, making it one of the most abundant polymers alongside cellulose, comprising 15–30 % of total plant biomass [22]. Lignin, with its aromatic rings, strongly absorbs ultraviolet light, but limited information exists regarding the synthesis, limitations, and applications of lignin-based composite materials in photocatalysis and photovoltaics [23]. Lignin-based composites have been used in solar cells such as for gel polymer electrolyte (GPE), which exhibit high ionic conductivity, enhanced Young's modulus, improved thermal stability, and strong electrochemical stability [24,25]. Lignin-based cross-linked materials have also been observed to significantly improve the long-term stability of quasi-solid-state dye-sensitized solar cells (QS-DSSC) under UV–Vis light compared to standard QS-DSSCs [26]. Moreover, the incorporation of lignosulfonate into conducting polymer blends enhances key properties such as conductivity, thermal stability, solubility, and mechanical strength [27].

Over the past decades, various researchers have reported differing photoconversion efficiencies (PCE) for DSSCs due to the effects of both metal and non-metal doping of TiO_2. Metal doping has resulted in an average PCE of 5.80 %, while non-metal doping has achieved an average PCE of 5.61 % [28]. In comparison, lignin-based doping, which does not show a significantly different PCE achievement, has an average PCE of 3.30 %, as shown in Table 4.

Lignin can act as a binding or reinforcing agent within the TiO_2 matrix. When used at the appropriate concentration, lignin enhances the mechanical stability of the material, making it more resistant to pressure or impact. It also improves the thermal stability of the polymer matrix by preventing thermal degradation [29]. Moreover, lignin has a high affinity for metal oxides, including TiO_2, which suggests it can form strong bonds with the TiO_2 surface [24]. Incorporating lignin from rice husk into TiO_2 is an attractive idea due to its lower environmental impact and potential to enhance the stability of DSSCs. However, its potential to improve the performance of TiO_2-based composites in DSSCs remains unexplored. While lignin from various natural sources has been investigated in recent studies [30–32], the modification of TiO_2 with rice husk lignin and comprehensive stability analyses of DSSC devices incorporating such materials have yet to be undertaken. This study aims to address these research gaps by evaluating the efficacy of rice husk lignin as a modifier for TiO_2-based photoanodes in DSSCs and performing stability analyses on the resulting devices. Detailed characterization was conducted to confirm the presence of lignin and evaluate the electrical performance of the solar cell devices [33]. Additionally, stability testing of the devices was conducted to assess their long-term performance. In addition, this research also seeks to enhance the recyclability of rice husk waste. This study not only aims to optimize the utilization of rice husk but also holds potential to significantly improve the efficiency and sustainability of renewable energy production, while addressing agricultural waste management.

2. Experimental

2.1. Chemicals and materials

In this study, rice husk (Oryza sativa) sourced from West Java, Indonesia, was used. Sodium hydroxide (NaOH, 98 %) was obtained

from Sakura Chemical, Indonesia. Materials including 18NR-AO Titania Paste (TiO_2), fluorine-doped tin oxide (FTO) conductive glass substrates (TEC-15; 15 Ω/sq sheet resistance, cut into 1.0 × 1.5 cm^2 pieces), ruthenium-based dye [$RuL_2(NCS)_2$]:2 tetra-n-butylammonium, where L = 2,2′-bipyridyl-4,4′-dicarboxylic acid (Z907), iodide-triiodide based high-performance electrolyte (EL-HPE), and low-temperature thermoplastic sealant (DuPont Surlyn®) were supplied by Greatcell Solar, Australia. Sulfuric acid (H_2SO_4, 98 %), ethanol (C_2H_5OH, ≥99.8 %), and titanium tetrachloride ($TiCl_4$) were sourced from Merck, Singapore. Additionally, a Teepol detergent solution was procured from Bratachem Indonesia.

2.2. Preparation of extraction lignin from rice husk

The following methods have been used to extract lignin from rice husks. For 4 h, rice husk powder was dissolved in 1 M NaOH solution at a weight to volume ratio of 1:12 (1 g of rice husk powder per 12 ml of NaOH solution) and stirred at an 80 °C. Then, until the neutral pH was reached, a solution from alkaline hydrolysis (AH) should be rinsed with deionized water. Next, the solid residue is manually decanted and the filtrate stored as an aqueous solution of lignin residues (black liquor). The filtrate was acidified by gradually adding 15 ml of 72 % H_2SO_4 solution until the pH reached 4 and left to stand until precipitation formed. Subsequently, dry the sample in an oven at 70 °C to remove any water content, as shown in Fig. 1a [34].

2.3. Fabrication of photoanode

Prior to the fabrication process, FTO was washed sequentially for 15 min using the mixture of Teepol detergent, deionized water, acetone, and ethanol. Next, the FTO glass was further cleaned using UV Ozone (Branson 3200 Ultrasonic Cleaner Waterbath) for 15 min. After UV treatment, FTO glass was immersed for 30 min at 70 °C in a 40 mM aqueous $TiCl_4$ solution (pre-$TiCl_4$). This process was followed by rinsing with deionized water and dried in oven at 120 °C for 10 min. The glass was then sintered at 500 °C for 30 min under air atmosphere.

For the preparation TiO_2 composite, the TiO_2 paste was dissolved in ethanol at the proportion of 2 g/ml, then followed by adding variations of lignin powder to the amount of the TiO_2 paste at the concentration of 2.5 %, 5 %, 7.5 %, 10 %, and 15 %, as can be seen in Fig. 1b. These materials were stirred at 60 °C for 4 h. The TiO_2–lignin solution was then deposited by spin coating method on treated FTO glass at 3500 rpm for 30 s (active area, 0.25 cm^2). The samples were then dried in an oven at 120 °C for 10 min before being annealed at 500 °C for 30 min. Following that, as a post-treatment step, the samples were immersed in a 40 mM $TiCl_4$ solution at 70 °C on a hot plate for 30 min, followed by 30 min of annealing at 500 °C. The samples were then submerged in a 100 mL ethanol solution containing 20 mg Ru-complex dye Z907 for 24 h at room temperature. Finally, the photoanodes were cleaned with ethanol and allowed to air dry.

2.4. Preparation of counter electrode

To fabricate the counter electrode, a 1 mm hole was first drilled in the upper right corner of the FTO glass for electrolyte filling. Platinum paste was then applied to the cleaned, perforated FTO glass, covering a 1.0 × 1.0 cm^2 area. The coated glass was dried in an oven at 120 °C for 10 min, followed by sintering at 500 °C for 30 min in an electric muffle furnace.

Fig. 1. Preparation of a) The water content removal of extracted rice husk result b) The composite of TiO_2 and lignin from rice husk.

2.5. DSSC assembly

The counter electrode and the prepared photoanode were assembled using a low-temperature thermoplastic sealant (DuPont Surlyn®) as a spacer and gently pressed with a hot press at 120 °C for 30 s. Liquid electrolyte (EL-HPE) was introduced through a 1 mm hole under vacuum. The hole on the counter electrode was then sealed with thermoplastic and aluminum foil. Finally, the components were firmly bonded through hot-press soldering of the strip.

3. Result and discussion

3.1. Fourier transform infrared (FT-IR)

The results of pure lignin, pristine TiO_2, TiO_2/lignin 5 %, and TiO_2/lignin 15 % were analyzed using FT-IR. FT-IR spectroscopy is useful for finding the presence of lignin components as an organic dopant in the semiconductor composite for the photoanode modification of DSSC. Fig. 2a shows the presence of the characteristic for vibration mode of TiO_2 (Ti–O stretching mode of Ti–O–Ti) at the wavenumber below approximately 800 cm^{-1} observed in pristine TiO_2 and the composite of TiO_2 and lignin [35]. Furthermore, the appearance of the bands in the range 1000 and 1400 cm^{-1} shows the existence of C–O or C–H, while the bands in the region of 1099–1107 cm^{-1} indicate the appearance of aromatic phenyl C–O found in pure lignin, TiO_2/lignin 5 %, and TiO_2/lignin 15 % that represents the typical structure of lignin with the higher vibration of the aromatic phenyl C–O, the higher Klason lignin content due to the degradation of hemicelluloses into pseudo-lignin [23,36].

Additionally, the intensity of the bands assigned to the C=O stretch of carbonyl groups and carboxyl groups (ca. 1600−1750 cm^{-1}), relative to the lignin aromatic band at 1633 cm^{-1}, and also found with less absorption intensity on pristine TiO_2 which is probably due to the remaining results from the interaction of ethanol (solvent) molecules which experience deprotonation of their hydroxyl groups, forming carbonyl (C=O) or carboxylic (COO^-) groups on the surface of TiO_2 [37].

Moreover, the characteristic bands located at 3440-3425 cm^{-1} indicate the existence of O–H stretching vibrations in aromatics that are found in pristine TiO_2, pure lignin, and the composite of TiO_2 and lignin [38]. TiO_2-lignin composites revealed absorption bands corresponding to both lignin and TiO_2, showing that lignin successfully formed a TiO_2-based composite. In addition, the presence of lignin components in the TiO_2 composite after the annealing process at a temperature of 500 °C indicates that lignin extracted from rice husk using the Klason method is categorized as not only a template but a dopant for TiO_2.

3.2. Thermogravimetric

The thermal properties of lignin-derived from rice husk using the Klason method were investigated through TGA in a nitrogen atmosphere, as illustrated in Fig. 2b. The study was performed at a heating rate of 10 °C/min, starting from room temperature and increasing to 600 °C, using 0.567 mg of powdered lignin. Fig. 2b displays the dynamic TGA, differential thermal analysis (DTA), and derivative thermogravimetry (DTG) curves. The thermal stability and decomposition temperature of the lignin powder were evaluated using TGA. The thermal decomposition of lignin occurs in three stages: the first stage, from room temperature to approximately 250 °C, results in a 10 % weight loss, primarily due to the degradation of bound water [39]. The second stage, between 250 and 350 °C, involves the breaking of α- and β-aryl-alkyl ether bonds and aliphatic chains, leading to an additional 30 % weight loss [40]. The third stage, from 350 to 600 °C, involves a 20 % weight loss due to the complete breaking of C-C bonds in lignin. Lignin extracted using the Klason method exhibits good thermal stability, attributed to extensive condensation during acid treatment, which enhances its thermal stability [41]. The DTA endothermic peak observed at 348.16 °C may be due to the dehydration or breakdown of lignin as a natural aromatic polymer. These findings indicate that the polymers exhibit strong thermal stability even at 500 °C, as evidenced by the

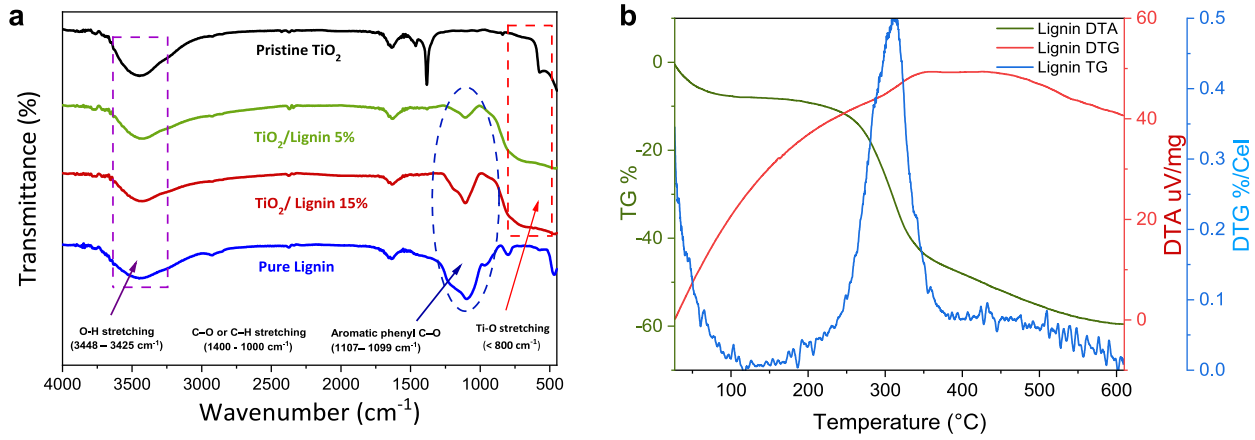

Fig. 2. a) FT-IR spectra of pure lignin, pristine TiO_2 and TiO_2/lignin 5 %, and TiO_2/lignin 15 % b) TG-DTG-DTA curve of pure lignin.

remaining lignin content, due to long conjugation and higher aromatic content in the polymer structure [42]. Furthermore, the temperature range of approximately 300–380 °C is associated with lignin, an amorphous polymer [43]. Thus, In the process of obtaining pure lignin from rice husk, it is crucial to isolate the hemicellulose and cellulose components. According to DTG analysis, hemicellulose decomposes primarily at 150–200 °C, while cellulose decomposes mainly at 200–300 °C [44,45]. However, lignin is more challenging to decompose. The weight loss observed in the temperature range of 300–380 °C is attributed to lignin, an amorphous polymer consisting of propane alcohol units such as O-H, C-H, and C-O (Fig. 2a). This structure makes lignin more stable and thus requires more heat energy for decomposition, as demonstrated in previous studies using the Klason method. The DTG data from rice husk extraction shows that lignin exhibits its maximum weight loss at 312.72 °C. Therefore, the successful extraction of rice husk lignin using the Klason method has been validated by the analysis of its thermal characteristics and corroborated by previous studies [46].

3.3. Scanning electron microscope (SEM)

The thin film surface morphology of the lignin-based modified photoanode, as depicted in Fig. 3 for each photoanode sample, shows some variations. In Fig. 3a, the pristine TiO_2 film exhibits smoother surface. On the other hand, TiO_2/lignin 5 % (Fig. 3b) demonstrates a smooth surface with several larger pores compared to the pristine TiO_2 surface, with additional pores spread across various parts of the surface, indicating a satisfactory increase in the surface area of the layer. Furthermore, the effectiveness of TiO_2 in the adsorption of dyes solutions is significantly enhanced by its higher porous structure, which allows for better contact between the dye solution and the TiO_2 surface. This is because the increased surface area provided by the porosity enables more efficient adsorption of the dye molecules onto the TiO_2 surface [47]. In addition, the enhancement of pore size can promote electrolyte directly flow to the surface of the semiconductor material before seeping outside.

3.4. Energy dispersive spectroscopy (EDS)

The Energy dispersive spectroscopy (EDS) analyses (Fig. 4a, b, and c) of pristine TiO_2, TiO_2/lignin 5 %, and TiO_2/lignin 15 % reveal the presence of Ti, O, Na, Si, and C, corresponding to the inner K shells of these elements. These shells are associated with electron emissions due to X-ray incidence. The weight percentages (wt%) of the primary peaks, titanium (Ti) and oxygen (O), which are the main elements of TiO_2, were determined. Elemental analysis shows titanium at 70.58 wt%, 68.83 wt%, and 53.92 wt%, and oxygen at 25.07 wt%, 24.08 wt%, and 37.03 wt%, respectively, demonstrating a reduction in oxygen content within the TiO_2 matrix following the addition of 5 % lignin than pristine TiO_2 [47]. The presence of strong peaks for titanium and oxygen in the spectrum confirms the purity of the TiO_2. Furthermore, a trace amount of sodium (Na) at 0.16 wt% was identified in the TiO_2/lignin 15 % composite, attributed to residual sodium hydroxide (NaOH) from the Klason extraction process [32]. The carbon (C) content showed an increase with lignin doping compared to pristine TiO_2, measured at 1.44 wt%, 3.66 wt%, and 3.43 wt%, respectively. Additionally, silicon (Si) was detected in all samples, with its weight percentage rising in tandem with higher lignin concentrations, measured at 2.27 wt%, 3.44 wt%, and 5.45 wt%, respectively.

3.5. Raman spectroscopy

To evaluate the phase identification of the nanocomposites, Raman spectroscopy was performed on pristine TiO_2, TiO_2/lignin 5 %, and TiO_2/lignin 15 %, as shown in Fig. 4d. The Raman spectra showed bands at 144 cm^{-1} (E_g), 196 cm^{-1} (E_g), 394 cm^{-1} ($B1_g$), 516 cm^{-1} ($B1_g$), and 638 cm^{-1} (E_g), indicating the anatase phase of TiO_2. Doping lignin into TiO_2 resulted in bands similar to undoped TiO_2, with an elimination in the small band at 321 cm^{-1} ($B1_g$), which is not characteristic band of anatase TiO_2 [48]. This phenomenon demonstrate that the presence of lignin alters the detected vibrational pattern and indicates that lignin modification results in covering the TiO_2 surface as shown in Fig. 3, thereby blocking the detection of unfamiliar peak in anatase TiO_2 [48].

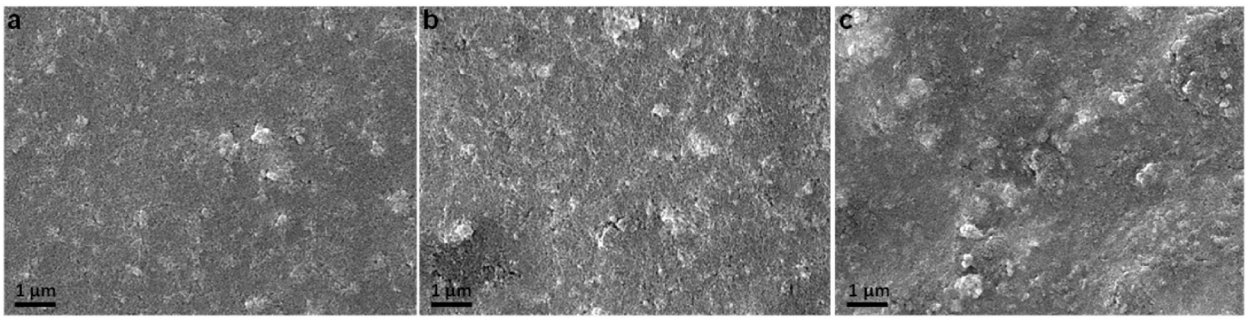

Fig. 3. SEM images of photoanode surface a) Pristine TiO_2 b) TiO_2/lignin 5 % c) TiO_2/lignin 15 %.

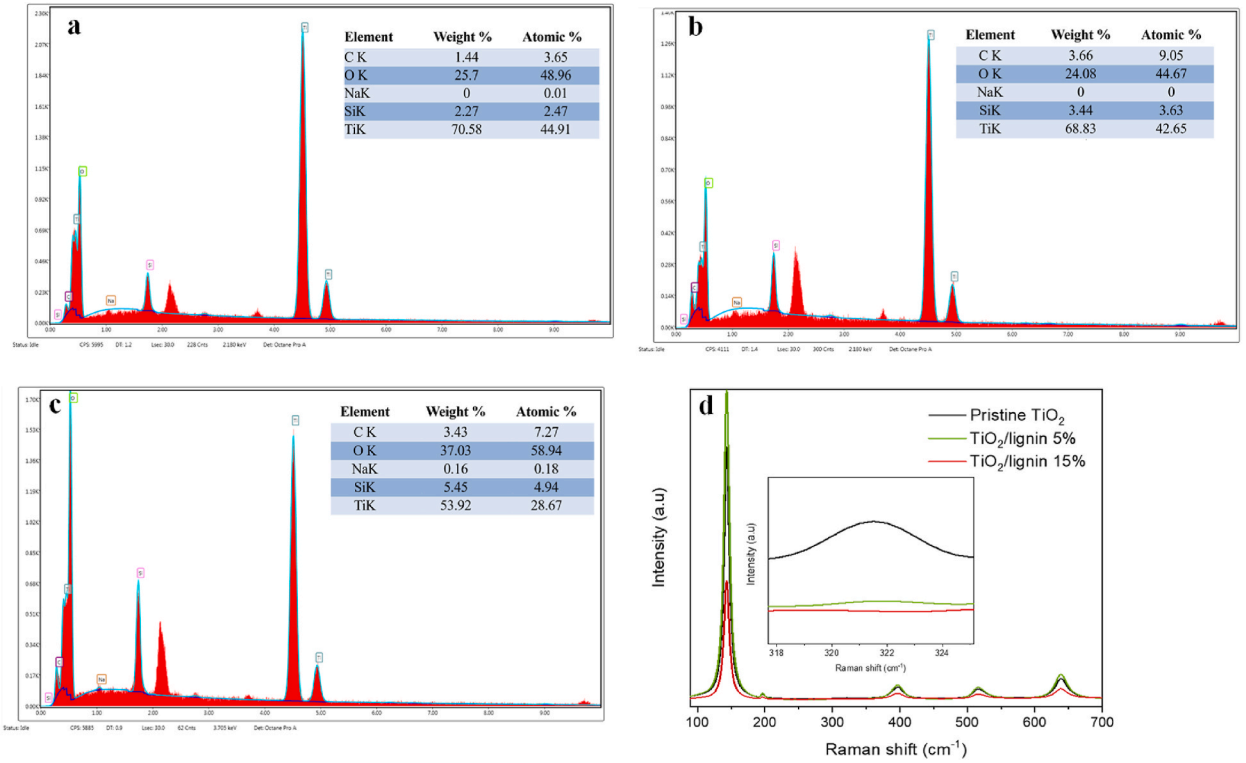

Fig. 4. EDS elemental analysis of a) Pristine TiO_2, b) TiO_2/lignin 5 %, c) TiO_2/lignin 15 %, and d) Raman spectra of pristine TiO_2, TiO_2/lignin 5 %, TiO_2/lignin 15 %.

3.6. Brunauer-emmett-teller (BET)

To elucidate the effect of lignin-doped for TiO_2 mesoporous, the BET surface area, pore volume, and pore size of pristine TiO_2, TiO_2/lignin 5 %, and TiO_2/lignin 15 % were evaluated by N_2 adsorption-desorption isotherm and the results as shown in Fig. 5 and Table 1. The pore distribution of pristine TiO_2 and TiO_2/lignin 5 % confirmed the increase of mesoporous size as shown in SEM images (Fig. 3), and the pore volume of TiO_2/lignin 5 % was increased compared to pristine TiO_2. The pore volume and BET surface area of TiO_2/lignin 5 % (0.47 cm^3/g and 61.8 m^2/g) were higher than that of the pristine TiO_2 (0.40 cm^3/g and 60.5 m^2/g), while the average pore size of TiO_2/lignin 5 % (15.3 nm) was higher than that of the pristine TiO_2 (13.1 nm). These could be attributed to the larger pores that were covered by adding lignin of 5%in TiO_2 paste, resulting in an increase in pore volume, BET surface area, and average pore size average pore size. Increasing the porosity of the TiO_2 surface may lead to improved interactions with surrounding dye and electrolyte solutions, as well as preventing electrolyte leakage leading to better utilization of active sites and faster kinetics which will result in a material being more stable for electrochemical reactions in DSSC applications [49]. Moreover, the TiO_2/lignin 5 % has a pore size of 15.32 nm which is considered as the optimal pore size for photoanode of DSSCs [50]. In addition, if the pore size is too small, there may not be enough surface area for effective dye loading. Conversely, TiO_2/lignin 15 % displayed a smaller pore volume (0.085 cm^3/g) and BET surface area (59.7 m^2/g) with a resulting in an increase in pore volume, BET surface area, and average pore size of 2.84 nm.

This reduction in pore size at higher lignin concentration is attributed to increased aggregation of lignin particles within the TiO_2 matrix, potentially blocking or occupying pore spaces as can be seen in Fig. 3. The TiO_2/lignin 5 % has a higher pore volume than pristine TiO_2 as shown in Fig. 4a. Higher pore volume suggest that adsorption is occurring more rapidly with increasing pressure in the given pore size range. Furthermore, the nitrogen adsorption isotherms of the samples are shown in Fig. 4b. In comparison to the pristine TiO_2, TiO_2/lignin 5 % shows a relatively high nitrogen adsorptive capacity at a P/P_0 range of 0–1. When there are more pores, it can be estimated that the dye absorption increases, and electrolyte leakage prevention occurs. Higher porosity results in higher specific capacitance as well as better cycling stability for electrochemical energy storage devices including DSSC [51]. In this case, the pore distribution of pristine TiO_2 and TiO_2/lignin 5 % confirmed the increase in pore size.

Moreover, The TiO_2/lignin 15 % was not plotted in both pictures due to limited tool capability for giving the data, the Barrett-Joyner-Halenda (BJH) model cannot be used to accurately estimate pore size less than 7.5 nm due to the limited validity of the Kelvin equation and neglect of fluid-wall interactions [52,53].

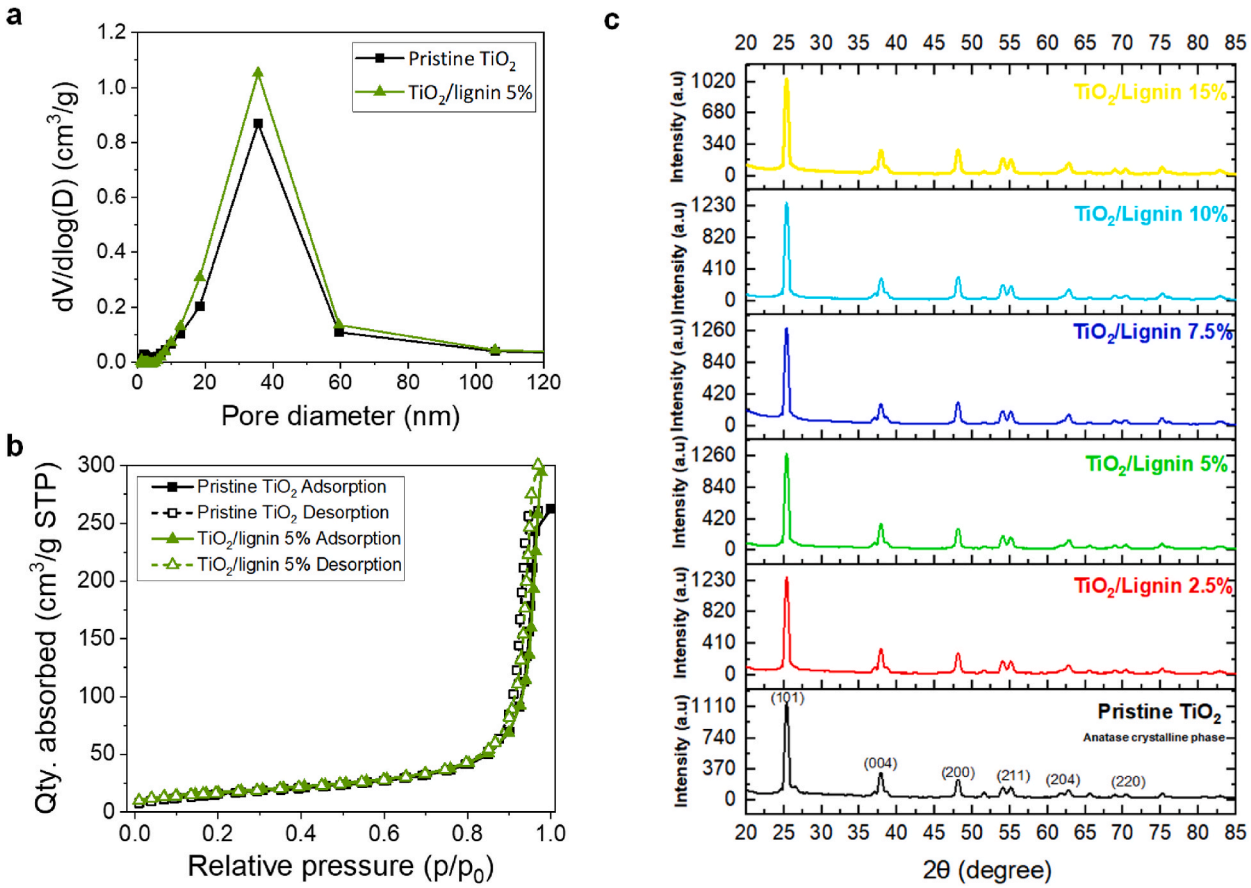

Fig. 5. a) Pore size distributions and b) N_2 adsorption-desorption isotherms of pristine TiO_2 and TiO_2/lignin 5 % c) XRD patterns of Pristine TiO_2 and TiO_2 composited within several lignin concentrations.

Table 1
Specific surface areas and calculated BET diameter of Pristine TiO_2, TiO_2/lignin 5 %, TiO_2/lignin 15 %.

No	Sample	BET surface area. S_{BET} ($m^2\ g^{-1}$)	Nitrogen pore volume ($cm^3\ g^{-1}$)	Average pore diameter (nm)
1	Pristine TiO_2	60.5	0.40	13.1
2	TiO_2/lignin 5 %	61.8	0.47	15.3
3	TiO_2/lignin 15 %	59.7	0.09	2.8

3.7. X-ray diffraction (XRD)

As shown in Fig. 5c, XRD diffractogram of TiO_2 exhibited the main peaks at 25.33°, 37.76°, 48.20°, 53.99°, 54.97°, 62.79°, 68.80°, 70.29°, 75.11° corresponding to (101), (004), (200), (105), (211), (204), (113), (220) and (215), which matched the tetragonal anatase structure of TiO_2 (JCPDS no. 21–1272) [54]. Furthermore, the (101) peak becomes more prominent in intensity compared to other peaks and the after incorporating lignin into the composite TiO_2. However, this intensity decreases when the lignin content reaches 15 %. Additionally, this increase of the crystalline size was attributed to the higher intensity of the most significant peak (101) [55]. This suggests that the original crystal cell structure of TiO_2 remains intact, with no additional crystalline by-products forming during the creation of the lignin/TiO_2 composite. Because lignin is inherently amorphous and lacks an ordered structure, the XRD diffractograms for both composites show no diffraction peaks attributable to lignin [56].

3.8. Transmission electron microscope (TEM)

TEM images of pristine TiO_2, TiO_2/lignin 5 %, and TiO_2/lignin 15 % were captured at two different scale bars. The images at 100 nm scale bars are shown in Fig. 6a, b, and 6c, while the images at 200 nm scale bars are presented in Fig. 6d, e, and 6f. The images

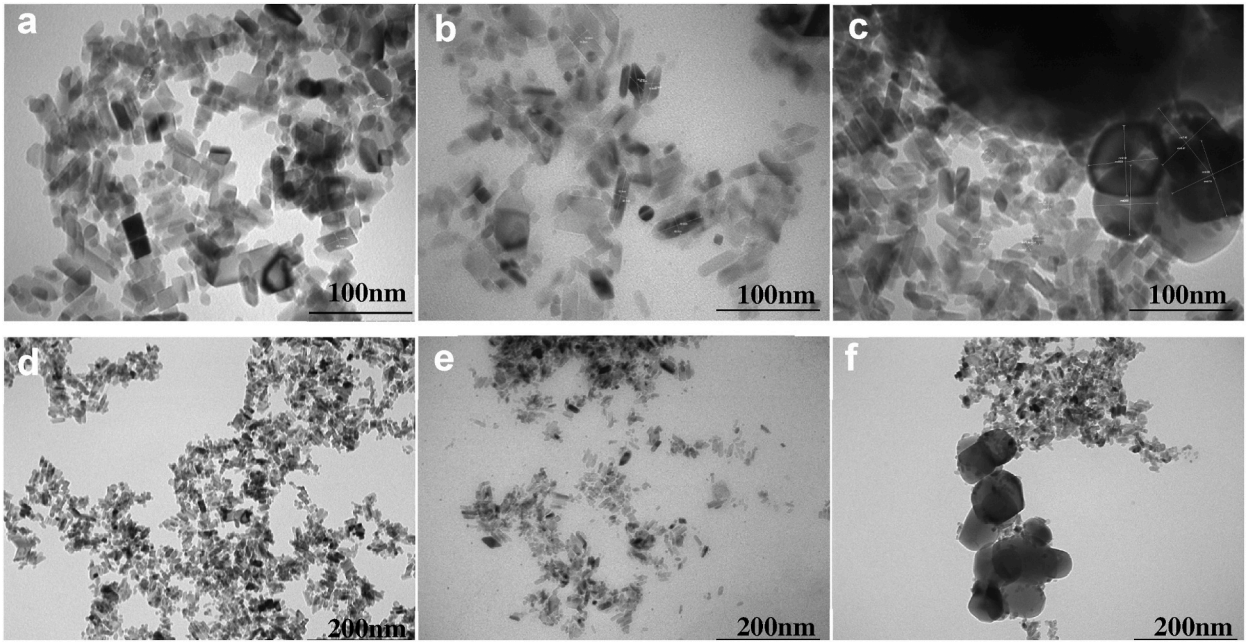

Fig. 6. TEM images of (a) pristine TiO_2, (b) TiO_2/lignin 5 %, (c) and TiO_2/lignin 15 % for scale bars correspond to 100 nm, and (d) pristine TiO_2, (e) TiO_2/lignin 5 %, (f) and TiO_2/lignin 15 % for scale bars correspond to 200 nm.

reveal variations in particle shape among the three samples. Pristine TiO_2 exhibits rod-like nanoparticles with an average size of about 12.67 × 25 nm. The addition of 5 % lignin to TiO_2 results in an increase in size of rod-like nanoparticles, with an average size of about 15.5 × 42 nm. Furthermore, increasing the lignin concentration to 15 % leads to the formation of uniform nanoparticles, including nanorods with an average size of about 12.33 × 12.33 nm, nanocubes with an average size of about 12.02 × 12.03 nm, and nanospheres with an average diameter size of about 63.10 nm, indicating the presence of aggregation due to the high lignin content in the TiO_2 composite, as confirmed by SEM observation.

3.9. Photoluminescence spectroscopy (PL)

The photoluminescence (PL) technique is extensively utilized to study oxygen vacancies, surface defects, surface states, charge recombination, and photo-induced charge separation in nanoscale semiconductor materials [57]. The PL spectrum of pristine TiO_2/Z907, TiO_2/lignin 5 %/Z907, and TiO_2/lignin 15 %/Z907 are shown in Fig. 7a with the peak at the wavelength around 785 nm

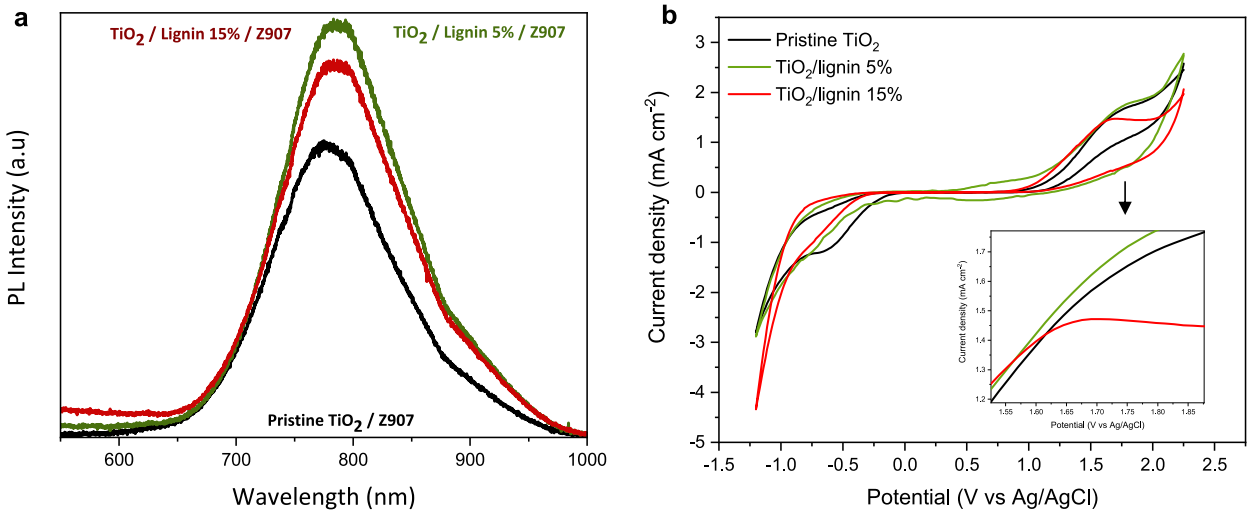

Fig. 7. The profile of a) Photoluminescence spectra of photoanode surface b) Cyclic voltammograms (CV) from Pristine TiO_2, TiO_2/lignin 5 %, TiO_2/lignin 15 % with adding dye Z907.

attributed to the PL peak of Z907 dye [58,59] The increase of PL intensity in TiO_2/lignin 5 %/Z907 was due to the expansion of the pores indicating that more dyes were adsorbed. The increase of dye adsorption on the TiO_2 surface increases the number of photons absorbed and stimulates more intense light emission. In addition, both TiO_2/lignin 5 %/Z907 and pristine TiO_2/Z907 might absorb not far for amounts of dye, but the structural differences due to lignin doping can influence electronic properties and recombination dynamics. Lignin doping modifies surface properties and electronic structure, potentially enhancing radiative recombination. Doping TiO_2 with 5 % lignin can reduce non-radiative defects. These defects act as recombination centers that quench photoluminescence by facilitating non-radiative pathways. With fewer non-radiative defects, more excitons recombine radiatively, increasing PL intensity [60].

Moreover, aggregation and grain size significantly affect optical properties. TiO_2/lignin 5 % has fewer aggregates compared to TiO_2/lignin 15 %, which shows more large aggregation. Large aggregates in TiO_2/lignin 15 % create localized defect states facilitating non-radiative recombination, reducing PL intensity. It is noted that the larger pore sizes in TiO_2/lignin 5 % (as shown in Table 1) are generally increased grain size, so the grain size in pristine TiO_2 is smaller than that in TiO_2/lignin 5 % which results in a higher defects concentration as shown in Fig. 6 [61]. These defects would act as non-radiative recombination centers and thus decrease the emission efficiency. Furthermore, Lignin doping can increase the density of oxygen vacancies, thus increasing radiative recombination and PL intensity [62,63]. Thus, although TiO_2/lignin 5 % absorbs more dye and increases the light emission of the PL peak, there can be a decrease in photovoltaic performance compared to pristine TiO_2 in the initial device measurements. This is due to an increase in recombination, which occurs because some electrons injected into the conduction band of TiO_2 return to the holes in the oxidized dye if the dye regeneration process, typically occurring on the microsecond time scale, is not fast enough [3,64]. This issue can be triggered by some dye molecules that have not interacted directly with TiO_2, as well as by the formation of lignin component aggregates.

Hence, this interaction explains why TiO_2/lignin 5 % shows the highest PL intensity, achieving a balance between sufficient lignin

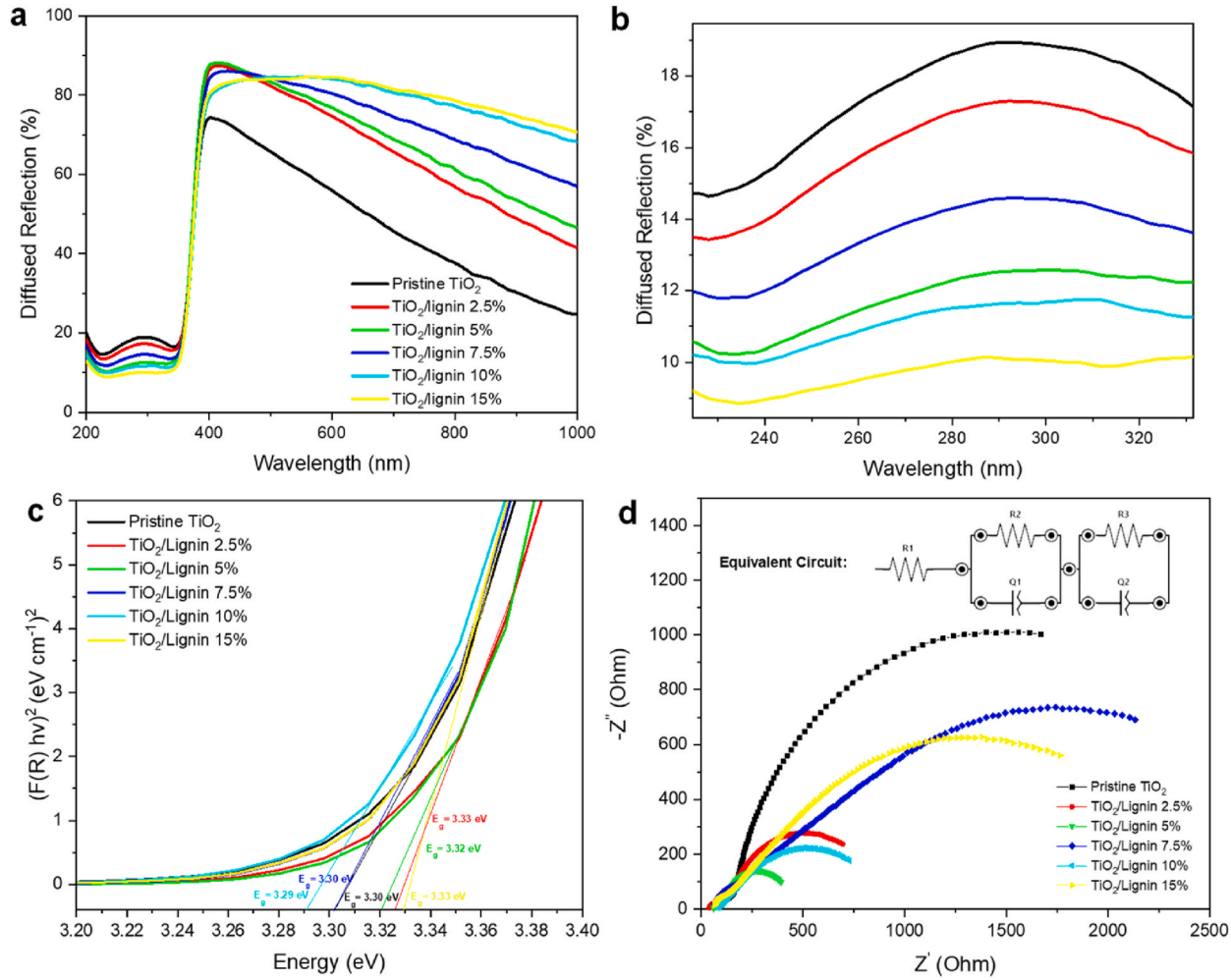

Fig. 8. The profile of a) UV–Vis Diffuse reflectance spectra in all region spectra, b) UV–Vis Diffuse reflectance spectra in UV spectra (c) Calculated band gaps based on Kubelka–Munk function for the photoanode of pristine TiO_2 and TiO_2 composited within several lignin concentrations without dye-sensitizer d) The EIS Spectra of pristine TiO_2, TiO_2/lignin 5 %, and TiO_2/lignin 15 %.

doping to reduce non-radiative defects and increase oxygen vacancies without causing excessive aggregation.

3.10. Cyclic voltammetry (CV)

To evaluate the cyclability of the composite photoanode, cyclic voltammetry (CV) curves were recorded for pristine TiO_2, TiO_2 with 5 % lignin, and TiO_2 with 15 % lignin. These measurements were conducted within a voltage range of −1.2 to +2.2 V vs. Ag/AgCl at room temperature, using a scan rate of 0.05 mV s^{-1}. The photoanodes were prepared by drop casting the samples. The electrolyte solution comprised 10 mM LiI, 1 mM I_2, and 0.1 M $LiClO_4$ in acetonitrile [65]. Fig. 7b presents the cyclic voltammetry analysis of these samples. The catalytic activity of photoanodes in both oxidation and reduction processes was investigated to evaluate the current response of the modified photoanodes. The voltammograms for pristine TiO_2, TiO_2/lignin 5 %, and TiO_2/lignin 15 % exhibited similar profiles, displaying electrochemical quasi-reversible waves indicating of redox phenomena in the photoanode.

The oxidation peak of TiO_2/lignin 5 % was observed at a potential of +1.73 V (vs. Ag/AgCl) with a peak current of 1.69 mA cm^{-2} which is slightly higher than that of pristine TiO_2 and TiO_2/lignin 15 %, with oxidation peaks at +1.67 and + 1.59 V (vs. Ag/AgCl), respectively, and peak currents of 1.54 and 1.39 mA cm^{-2}, respectively. This increase in peak current for TiO_2/lignin 5 % indicates enhanced electron transfer kinetics [66]. Additionally, the electrocatalytic reduction shows that pristine TiO_2 has a clear peak potential at −0.6 V, which is higher than that of TiO_2/lignin 5 % and TiO_2/lignin 15 %. Thus, the higher oxidation peak demonstrates higher electrolyte absorption.

3.11. UV–Vis diffuse reflectance

The photoanode's reflectivity was examined to study the scattering impact of TiO_2 and lignin composite. The diffuse reflectance UV–Vis spectra in Fig. 8b were used to analyze the reflectivity intensity before dye absorption in the photoanode film. It was observed that the reflectivity intensity is higher in TiO_2 composites with increased lignin concentration compared to pristine TiO_2 in the 400–800 nm wavelength range. This is indicative of larger particle size in TiO_2/lignin composite, which has better light scattering properties. Moreover, the results also indicate that incident light is significantly scattered within the larger particles, contributing to improved DSSC performance by utilizing sunlight more effectively [67]. Moreover, increasing lignin concentrations lead to the growth of various particle sizes, as previously reported [68]. The previous report indicated that similar scattering effects were produced by different-sized particles. However, it is important to note that different particle sizes may have adverse effects due to particle aggregation. Excessive particle size caused by aggregation can result in reduced dye adsorption, and larger particles may obstruct part of the TiO_2, diminishing the accessible internal surface area, as observed in the 15 % TiO_2/lignin composite with diverse particle sizes (aggregates) depicted in Fig. 6f. In addition, the observed enhancement in reflectance is attributed to the increased porosity, which results in a larger surface area and better dispersion of lignin particles within the mesoporous TiO_2, as illustrated in Table 1. The incorporation of lignin into the TiO_2 matrix introduces additional porosity due to the inherent structure of lignin, which is rich in voids and channels as shown in Fig. 3. This structural characteristic of lignin contributes to the formation of a more porous TiO_2 composite, thereby increasing the overall surface area. Furthermore, the TiO_2 with adding lignin 5 %, the dispersion of lignin particles within the TiO_2 matrix prevents the agglomeration of TiO_2 nanoparticles, increasing surface area. The lignin acts as a spacer, ensuring the TiO_2 particles remain well-dispersed and do not cluster together. This improved dispersion enhances the accessibility of the TiO_2 surface for light interaction, leading to increased reflectance and light scattering. Additionally, the presence of lignin particles dispersed in TiO_2 is validated through EDS analysis (Fig. 4a, b, c). The EDS results demonstrate that with higher lignin doping concentrations, the total TiO_2 component decreases within the same active area detection. This indicates that lignin is effectively incorporated into the TiO_2 matrix, altering its composition and surface characteristics. Contrastingly, excessively high lignin concentrations can adversely affect the photovoltaic performance of DSSCs. This is primarily due to the significant coverage of the active area by lignin, which does not correspond with a sufficient increase in porosity. The poor homogeneity of the TiO_2/lignin composite at high lignin concentrations leads to the formation of numerous aggregations. These aggregations, particularly evident in the TiO_2/lignin 15 %, hinder the efficient operation of the DSSC and lead to reduced photovoltaic performance. Thus, increasing the lignin concentration leads to an increase in diffuse reflectance, marked by a decrease in TiO_2 components and an increase in detected lignin concentration.

Moreover, absorbance analysis also can be interpretated using UV-DRS in UV and visible region as shown in Fig. 8b. In the UV region, an increase in lignin concentration shifts the absorption range, leading to stronger light absorption than that of pristine TiO_2, which indicated that lignin-TiO_2 had good UV-shielding property [69,70].

Furthermore, the band gaps of the photoanodes based on pristine TiO_2 and TiO_2 composited within several lignin concentrations were calculated to be 3.30 eV (pristine TiO_2), and 3.33, 3.32, 3.30, 3.29, 3.33 eV (respectively) according to the Kubelka–Munk function (Fig. 8c), indicating that the presence of lignin generated an impurity band and narrowed the band gap of TiO_2, without exerting a significant impact.

The Kubelka–Munk (K-M or F(R)) technique for measuring the bandgap of solid materials using DRS results, The K–M method is based on the following equation (1):

$$F(R) = \frac{(1-R)^2}{2R} \tag{1}$$

where R is the reflectance; F(R) is proportional to the extinction coefficient (α). This equation is typically applied to materials that are both highly reflective and absorbent. By substituting F(R) in Eq. (1), the bandgap can be determined from the reflectance data. TiO_2

exhibits both direct and indirect bandgap. However, it is proved that indirect bandgap is favoured in anatase TiO_2 [71]

3.12. Electrochemical Impedance spectroscopy

. EIS was performed on DSSC devices as illustrated in Fig. 8c. The Nyquist plots displayed two semicircular arcs. The electrode potential losses originate from three main sources: ohmic, activation, and mass transfer losses [72]. Consequently, the equivalent circuit model $R_1(R_2Q_2)(R_3Q_3)$ was utilized to analyze the internal resistance components. In this circuit, R_1 represents the ohmic resistance, R_2 and Q_2 in parallel signify the combined activation resistance and the double-layer capacitance for the anode and cathode, while R_3 and Q_3 in parallel correspond to the finite diffusion effects [73]. In general, the small semi-circle observed in the high-frequency region is attributed to the redox reaction occurring between the electrolyte and the Pt interface. Meanwhile, the large semi-circle in the middle-frequency region is associated with electron transfer at the TiO_2–dye–electrolyte interface [74]. The pristine TiO_2 exhibits the largest semicircles among the TiO_2 composites with various lignin concentrations in both high-frequency and low-frequency regions. This is primarily due to the low amount of electrolyte adsorption, resulting in fewer ions available for charge transfer, as indicated by increased Charge Transfer Resistance (Rct/R_3). Moreover, the TiO_2/lignin 5 % composite showed the smallest semicircles, which could be attributed to its role as a higher scattering layer, leading to better light scattering effects than pristine TiO_2. In summary, the TiO_2/lignin 5 % composite, with its smaller essential resistance, indicates that the as-prepared TiO_2 nanotubes constructed higher mesoporous are suitable for improving photoanode efficiency. However, the presence of slight aggregates may slightly reduce its I-V performance at the first measurement (Fig. 9a). Additionally, other devices with added lignin show intermediate semicircle sizes due to suboptimal pore enhancement and the presence of larger aggregates in the TiO_2/lignin 15 % composite (Fig. 3c). This EIS measurement was conducted immediately after each device was injected with the electrolyte solution. Thus, the increase in pore size in the TiO_2/lignin 5 % resulted in more optimal electrolyte absorption compared to pristine TiO_2 as confirmed by CV measurement.

3.13. DSSC characterization

Next, the photovoltaic properties of DSSCs with lignin-modified photoanodes were investigated. These photoanodes included pristine TiO_2 and TiO_2 composited with varying concentrations of lignin. J-V measurements were employed to evaluate the electrical properties of DSSC using a sun simulator with a Xenon lamp as the light source. As shown on Table 2, It can be seen that the modified photoanode of DSSC with the pristine TiO_2 as the control device shows a short-circuit current (J_{SC}) of 14.35 mA cm^{-2}, an open-circuit voltage (V_{OC}) of 0.661 V, and a fill factor (FF) of 53.4 %, resulting in a power conversion (PCE) of 5.07 %. The modified photoanode of DSSC using TiO_2/lignin 5 % shows not far performance from the pristine TiO_2, a J_{SC} of 12.56 mA cm^{-2}, a V_{OC} of 0.669V, and a FF of 57.3 %, resulting in a PCE of 4.81 %. Moreover, the TiO_2/lignin 15 % for the highest concentration shows the performance with a J_{SC} of 8.69 mA cm^{-2}, an V_{OC} of 0.669V, and a FF of 55.5 %, resulting in a PCE of 3.22 %.

The lower PCE of the TiO_2 and lignin composite at various concentrations compared to pristine TiO_2 is primarily due to the decrease in Jsc, as shown in Table 2. This reduction in Jsc can be attributed to the presence of lignin, which may reduce the available TiO_2 surface sites for dye adsorption despite the increase in TiO_2 nanoparticle size. Additionally, lignin might introduce barriers that hinder electron transfer, increase recombination rates, and alter the composite's optical properties, leading to less effective light harvesting. These factors collectively contribute to the observed decrease in Jsc and, consequently, the PCE. However, using a 5 % lignin concentration appears optimal, as it increases the pore size in the TiO_2 mesoporous structure, allowing for more dye adsorption without significantly reducing Jsc due to minimal aggregation. This enhanced pore structure facilitates deeper dye penetration, substituting degraded dye molecules that directly interacted with TiO_2 in the first measurement, thereby maintaining PCE stability for three months.

After the first measurement and stored for one month, the DSSC performance was characterized as also presented in Table 2 and visually represented in Fig. 9a using J-V curve. In Fig. 9a, it is evident that when compared to pristine TiO_2, all lignin-doped devices

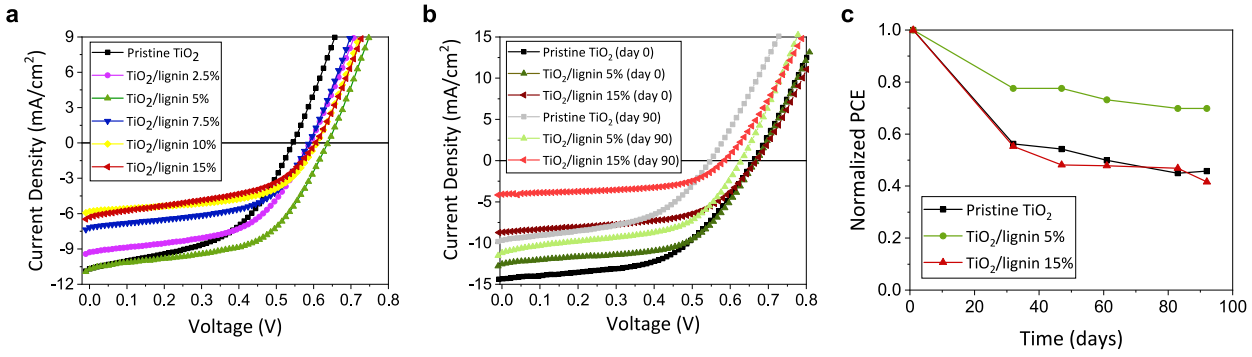

Fig. 9. The J-V Curve of Pristine TiO_2, TiO_2/lignin 5 %, and TiO_2/lignin 15%in DSSCs performance investigation for a) 1 month b) 3 months c) Long-term stability assessment for a 3-month investigation.

Table 2
Photovoltaic parameters of DSSC for the Pristine TiO_2 and TiO_2 composited within several lignin concentrations in the first measurement and after one month storage.

No	Photoanode	Day 0			PCE	Day 30			PCE
	Sun (100 mW/cm^2 AM 1.5G)	FF	V_{OC}	J_{SC}		FF	V_{OC}	J_{SC}	
		(%)	(V)	(mA/cm^2)	(%)	(%)	(V)	(mA/cm^2)	(%)
1	Pristine TiO_2	53.4	0.661	14.35	5.07	49.0	0.545	10.69	2.85
2	TiO_2/Lignin 2.5 %	57.1	0.660	10.67	4.02	53.6	0.590	9.28	2.93
3	TiO_2/Lignin 5 %	57.3	0.669	12.56	4.81	54.6	0.638	10.72	3.73
4	TiO_2/Lignin 7.5 %	53.0	0.666	11.59	4.09	54.6	0.587	7.18	2.31
5	TiO_2/Lignin 10 %	55.7	0.656	7.98	2.92	56.4	0.609	5.82	2.0
6	TiO_2/Lignin 15 %	55.5	0.669	8.69	3.22	46.8	0.605	6.30	1.78

exhibit J-V curves with a more rectangular shape, indicative of enhanced fill factor (FF). Notably, the addition of 5 % lignin to the TiO_2 composite resulted in the best performance that demonstrates the improved stability for the lignin-doped devices: the PCE of 3.75 %, the V_{OC} of 0.638V, the FF of 54.6 %, and the J_{SC} achieved at 10.72 mA/cm^2. In comparison, the pristine TiO_2 exhibited smaller values: PCE of 2.85 %, V_{OC} of 0.545V, FF of 49 %, and J_{SC} of 10.69 mA/cm^2.

In addition, the stable performance of the TiO_2/lignin 5 % was also confirmed as shown in Fig. 9b. The J-V curve for TiO_2/lignin 5 % exhibited minimal deviation after 3 months storage. The device maintained a steady peak current density, with a slighter decrease from 12.56 to 9.77 mA/cm^2. Moreover, TiO_2/lignin 15 % experienced a second small decrease from 8.69 to 4.08 mA/cm^2, while pristine TiO_2 exhibited the highest decrease from 14.3 to 9 mA/cm^2. The consistent light absorption and charge generation by the dye molecules in TiO_2/lignin 5 % were reflected in their slower decline over time. Moreover, the third month of J-V curve shows that TiO_2/lignin 5 % has the closest resemble a rectangle than pristine TiO_2 and TiO_2/lignin 15 % indicating that it has high V_{OC}, high J_{SC}, and a high FF.

Advanced investigation of aging tests were conducted on lignin from rice husk on TiO_2 on the modified photoanode of DSSC for around 90 days and displayed the parameters of the best stability performance on three devices including PCE, J_{SC}, V_{OC} and FF (normalized). The PCE stability of photoanodes over an extended aging period was investigated as shown in Fig. 9c and Table 3. The device using pristine TiO_2 on the photoanode exhibited poor stability, with a 48 % decrease in power conversion efficiency (PCE) over 90 days due to the absence of a polymer matrix that can avoid electrolyte evaporation or leakage from sealing imperfections. In addition, the TiO_2/lignin 15 % device yield performance, with an initial PCE of 3.22 % on the first day, decreasing to 1.55 % after 90 days (51 % reduction). However, the TiO_2/lignin 5 % device achieved better stability, maintaining an initial PCE of 4.81 % and experiencing only a slight decrease to 3.36 % after 90 days (a reduction of 22 %). As shown in S1a, the TiO_2/lignin 5 % exhibits greater V_{OC} stability compared to TiO_2/lignin 15 %, while pristine TiO_2 has the poorest stability. Furthermore, as can be seen from S1b,c, TiO_2/lignin 5 % is more stable J_{SC} and FF than pristine TiO_2 and TiO_2/lignin 15 %.

Specifically, the favorable characteristics of the lignin-modified photoanode with 5 % concentration include the higher pore distribution namely 15.32 nm compared to pristine TiO_2 (13.13 nm), well-ordered mesoporous that facilitate mass transport, an increased surface area providing more sites for dye adsorption, that aids in the separation of photogenerated electron-hole pairs, as confirmed by surface photovoltage measurements [75].

Additionally, the hydroxyl groups in lignin, along with other functional groups such as carboxyl and carbonyl (as shown in the FTIR spectra in Fig. 2a, are essential for specific interactions with functional component precursors. These hydroxyl groups can form hydrogen bonds with the hydroxyl groups on the surface of TiO_2 particles. Hydrogen bonding occurs when a hydrogen atom, covalently bonded to an electronegative atom like oxygen in –OH, interacts with another electronegative atom, enhancing adhesion between lignin and TiO_2 [76]. Notably, $TiCl_4$ is used as both a pre- and post-treatment in DSSCs to improve cohesion on the TiO_2 surface. The strongly electronegative hydroxyl groups on the lignin surface have a high affinity for electropositive metal ions. Specifically, the positively charged $Ti(OH)_n^{(4-n)+}$ species, formed during the partial hydrolysis of $TiCl_4$, readily binds to nucleophilic ligands, facilitating adsorption onto the lignin surface through electrostatic attraction. This adsorbed $Ti(OH)_n^{(4-n)+}$ then undergoes further hydrolysis and transforms into Ti–(O–lignin)$_4$, resulting in the formation of uniformly distributed TiO_2 nanoparticles on the lignin surface [77]. Based on our finding, the addition of various lignin concentrations did not significantly degrade performance, highlighting its compatibility and potential for use in these applications. Furthermore, DSSC devices incorporating TiO_2/lignin 5 % exhibit efficiency levels nearly equivalent to pristine TiO_2, simultaneously enhancing device stability. Optimizing homogeneity during the stirring process leads to further efficiency improvements, as it minimizes the presence of aggregated particles, which could otherwise act as a

Table 3
The DSSC performance of 3-month operation for the Pristine TiO_2, TiO_2/lignin 5 % and TiO_2/lignin 15 %.

No	Photoanode	Day 90			PCE (%)
	Sun (100 mW/cm^2 AM 1.5G)	V_{OC} (V)	FF (%)	J_{SC} (mA/cm^2)	
1	Pristine TiO_2	0.557	47.7	9.0	2.39
2	TiO_2 + Lignin 5 %	0.624	55.2	9.77	3.36
3	TiO_2 + Lignin 15 %	0.584	56.1	4.08	1.34

Table 4
Latest research of modifying photoanode using lignin in DSSCs.

No	Lignin source	Deposition Technique	Layer type	Dye-sensitizer	Counter electrode	PCE (%)	Stability	Year	Ref.
1	The self-growing plant (Typha Angustifolia)	Doctor blade	Single layer composite material	Fresh flowers (Raspberry)	Graphite	2.95	Not reported	2020	[30]
2	The self-growing plant (Lily)	Doctor blade	Single layer composite material	N719	Graphite	2.3	Not reported	2021	[31]
3	Commercial lignin	Spin coating	Double layer	N719	Platinum	4.65	Not reported	2022	[32]
4	Rice husk	Spin coating	Single layer composite material	Z907	Platinum	4.81	Reported	This work	

potential source of resistance.Furthermore, the degradation of electrolytes in DSSCs can be effectively mitigated through lignin doping.

After completing the characterization process using a sun simulator and storing the devices for 90 days, advanced stability evaluation of these device was tested under an LED-powered Dyenamo Toolbox. Specifically, The transient photo-voltage (TPV) method, a transient technique, was employed to investigate carrier recombination processes in our DSSCs. TPV induces a small Fermi level change within the solar cell. In contrast, V_{OC} decay captures the complete decay from a specific light intensity down to zero V_{OC}, effectively measuring all changes over time. Additionally, the working dynamic range for determining recombination kinetics in thin-film solar cells was aimed to be identified [78,79].

The V_{OC} decay was measured for DSSCs with various samples: pristine TiO_2, TiO_2/lignin 5 %, and TiO_2/lignin 15 %, using TPV as depicted in S2. Notably, as light intensity increases, the V_{OC} of the solar cell also rises, resulting in a faster decay rate with a consistent trend across all devices. Furthermore, different light biases were used to compare these decay kinetics, as represented in Fig. 10. By correlating changes in V_{OC} with carrier lifetime extracted from TPV measurements using equation (2):

$$\delta V = Ae^{-t/\tau}$$

where τ (s) represents the charge carrier lifetime and t is the time [80].

Additionally, the open-circuit potential decay transients of dye-sensitized nanostructured TiO_2 solar cells were examined (shown in Fig. 10a). When the light source was switched off at = 0 s, the voltage of cells with pristine TiO_2 or TiO_2/lignin 15 % dropped to less than 300 mV after 10 s. In addition, this phenomenon of the open-circuit potential decay transients was clarified in Fig. 10b. Remarkably, cells with TiO_2/lignin 5 % maintained a voltage of over 300 mV. Notably, the traces for pristine TiO_2 and TiO_2/lignin 5 % cells were approximately parallel, while the TiO_2/lignin 15 % cell exhibited distinct decay behavior. Furthermore, the observed trends in small modulation square wave (SW) photocurrent/voltage transients, as shown in Fig. 10c, indicated that with an increase in base light intensity, carrier lifetimes tended to decrease. Thus, the TPV and V_{OC} decay measurements revealed that the incorporation of lignin into TiO_2 affects the recombination dynamics in DSSCs. Specifically, TiO_2/lignin 5 % showed improved charge retention and slower recombination rates compared to pristine TiO_2 and TiO_2/lignin 15 %. The results indicate that moderate lignin doping (5 %) enhances the performance of DSSCs by improving carrier lifetimes and reducing recombination rates. Conversely, higher lignin content (15 %) may introduce distinct recombination behaviors, potentially due to several aggregation, negatively impacting the device's performance.

In the past decade as summirized in Table 4, the number of publications discussing the stability of DSSC modules has noticeably declined compared to the 2005–2010 period [3]. Additionally, the adoption of natural doping agents, such as lignin, remains relatively low. This research demonstrates that rice husk lignin enhances DSSC performance and includes stability testing, marking a well and novel improvement over previous lignin-based doping research conducted about the last five years.

4. Conclusions

The utilization of lignin extracted from rice husk as a novel natural dopant and biopolymer template in photoanode modification for DSSCs holds significant promise. Lignin, being abundant and sustainable, enhances the eco-friendliness of DSSCs. This study explores the impact of various concentrations of rice husk lignin, extracted using the Klason method. Incorporating lignin-doped TiO_2 improves UV–Vis light absorption and maintains the TiO_2 crystal structure, with chemical bonding between TiO_2 and lignin. Doping TiO_2 with 5 % lignin achieved a PCE of 4.81 %, demonstrating enhanced stability. This enhancement is attributed to the increased pore size and uniform pore distribution on the TiO_2 film, which improves dye and electrolyte collection, thereby prolonging DSSC performance. The TiO_2/lignin 5 % device maintains stable performance, showing a 22 % lower reduction in PCE, V_{OC} and J_{SC} compared to pristine TiO_2 and TiO_2/lignin 15 % over a 3-month period. Additionally, TiO_2/lignin 5 % exhibits the slowest decrease in stability over time.

CRediT authorship contribution statement

Gita Rabelsa: Writing – original draft, Methodology, Investigation, Data curation. **Shobih:** Writing – review & editing, Investigation, Formal analysis, Writing – review & editing, Investigation, Formal analysis. **Jojo Hidayat:** Resources, Investigation. **Phutri**

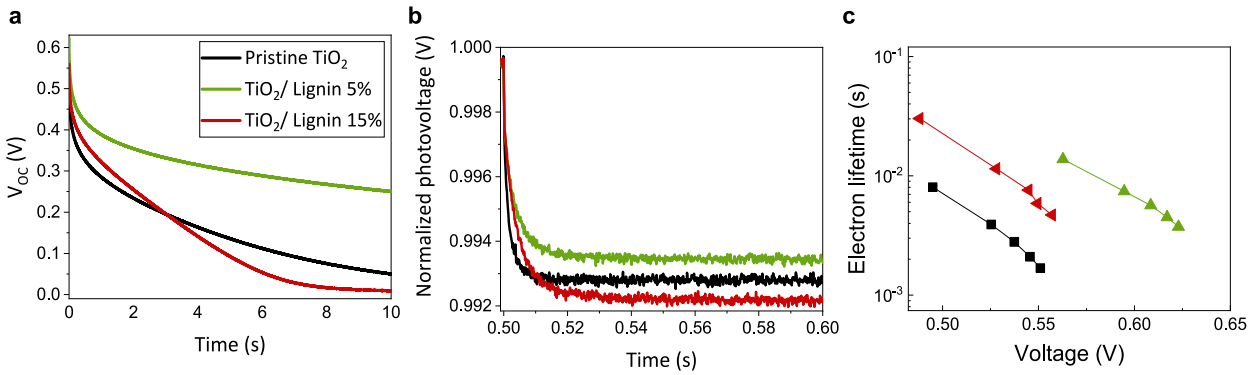

Fig. 10. Performance evaluation after three months of a) Decay transients of the open-circuit potential by carrier b) decay transients of the open-circuit potential. c) Carrier lifetime of pristine TiO_2, TiO_2/lignin 5 % and, TiO_2/lignin 15 %.

Milana: Writing – review & editing, Validation, Formal analysis. **Widhya Budiawan:** Writing – review & editing, Investigation, Formal analysis. **Erdin Almuqqodas:** Methodology, Investigation. **Natalita M. Nursam:** Writing – review & editing, Supervision, Resources. **Ahmad Ibrahim:** Supervision, Formal analysis. **Lia M. Pranoto:** Resources, Formal analysis. **Yuliar Firdaus:** Writing – review & editing, Supervision, Formal analysis. **Brian Yuliarto:** Writing – review & editing, Funding acquisition, Conceptualization.

Data availability

Data will be made available on request.

Declaration of competing interest

The authors declare that they have no known competing financial interests or personal relationships that could have appeared to influence the work reported in this paper.

Acknowledgements

The author (Gita Rabelsa) thanks BRIN Research Assistant (No. 60/II/HK/2023) and Degree by Research Program (No. 17/HK/II/2023). This research project was funded by Riset dan Inovasi untuk Indonesia Maju or RIIM program LPDP-BRIN (No. 82/II.7/HK/2022).

Appendix A. Supplementary data

Supplementary data to this article can be found online at https://doi.org/10.1016/j.heliyon.2024.e39913.

References

[1] A.N. Kay Lup, V. Soni, B. Keenan, J. Son, M.R. Taghartapeh, M.M. Morato, Y. Poya, R.M. Montañés, Sustainable energy technologies for the Global South: challenges and solutions toward achieving SDG 7, Environmental Science: Advances 2 (2023) 570–585, https://doi.org/10.1039/d2va00247g.
[2] A.B. Muñoz-García, I. Benesperi, G. Boschloo, J.J. Concepcion, J.H. Delcamp, E.A. Gibson, G.J. Meyer, M. Pavone, H. Pettersson, A. Hagfeldt, M. Freitag, Dye-sensitized solar cells strike back, Chem. Soc. Rev. 50 (2021) 12450–12550, https://doi.org/10.1039/d0cs01336f.
[3] A.B. Muñoz-García, I. Benesperi, G. Boschloo, J.J. Concepcion, J.H. Delcamp, E.A. Gibson, G.J. Meyer, M. Pavone, H. Pettersson, A. Hagfeldt, M. Freitag, Dye-sensitized solar cells strike back, Chem. Soc. Rev. 50 (2021) 12450–12550, https://doi.org/10.1039/d0cs01336f.
[4] A. Hagfeldt, G. Boschloo, L. Sun, L. Kloo, H. Pettersson, Dye-sensitized solar cells, Chem. Rev (2010) 6595–6663.
[5] F. Kong, S. Dai, K. Wang, Review of recent progress in dye-sensitized solar cells. Advances in OptoElectronics, 2007, https://doi.org/10.1155/2007/75384.
[6] G.Z. Li, S. Zhang, D. Tian, G. Liu, W. Wang, G. Chen, J. Wang, W. Wan, C. Yang, H. Yu, R. Han, Improving the visible light absorption and photocatalytic degradation activity of TiO2 particles towards MB by organic sensitizer decoration, Catal Letters 154 (2024) 3896–3910, https://doi.org/10.1007/s10562-024-04622-0.
[7] Q. Liu, J. Wang, Dye-sensitized solar cells based on surficial TiO2 modification, Sol. Energy 184 (2019) 454–465, https://doi.org/10.1016/j.solener.2019.04.032.
[8] B. Roose, S. Pathak, U. Steiner, Doping of TiO2 for sensitized solar cells, Chem. Soc. Rev. 44 (2015) 8326–8349, https://doi.org/10.1039/c5cs00352k.
[9] K. Sahu Dhonde, M. Dhonde, V.V.S. Murty, Novel synergistic combination of Al/N Co-doped TiO2 nanoparticles for highly efficient dye-sensitized solar cells, Sol. Energy 173 (2018) 551–557, https://doi.org/10.1016/j.solener.2018.07.091.
[10] A. Gupta, K. Sahu, M. Dhonde, V.V.S. Murty, Novel synergistic combination of Cu/S co-doped TiO2 nanoparticles incorporated as photoanode in dye sensitized solar cell, Sol. Energy 203 (2020) 296–303, https://doi.org/10.1016/j.solener.2020.04.043.
[11] M. Dhonde, K. Sahu Dhonde, K. Purohit, V.V.S. Murty, Facile synthesis of Cu/N co-doped TiO2 nanoparticles and their optical and electrical properties, Indian J. Phys. 93 (2019) 27–32, https://doi.org/10.1007/s12648-018-1275-4.

[12] M. Dhonde, K. Sahu, V.V.S. Murty, Cu-doped TiO2 nanoparticles/graphene composites for efficient dye-sensitized solar cells, Sol. Energy 220 (2021) 418–424, https://doi.org/10.1016/j.solener.2021.03.072.
[13] A. Mujawar, K. Shaikh, P. Lokhande, A. Supekar, N. Naik, S. Kowshik, S. Jadkar, Effect of nickel oxide concentration on titanium oxide bilayer photoanode for dye-sensitized solar cell application, J. Mater. Sci. Mater. Electron. 35 (2024), https://doi.org/10.1007/s10854-024-13141-y.
[14] U. Mahajan, K. Prajapat, K. Sahu, P. Ghosh, P.M. Shirage, M. Dhonde, Unveiling the impact of TiCl4 surface passivation on dye-sensitized solar cells: enhancing charge transfer kinetics and power conversion efficiency, J. Mater. Sci. Mater. Electron. 34 (2023), https://doi.org/10.1007/s10854-023-11555-8.
[15] A. Gok, Reliability and Ecological Aspects of Photovoltaic Modules Edited by Abdülkerim Gok, IntechOpen, London, United Kingdom, 2020.
[16] R. Purbia, R. Borah, S. Paria, Carbon-doped mesoporous anatase TiO2 multi-tubes nanostructures for highly improved visible light photocatalytic activity, Inorg. Chem. 56 (2017) 10107–10116, https://doi.org/10.1021/acs.inorgchem.7b01864.
[17] J. Li, L. Gao, W. Gan, Bioinspired C/TiO2 photocatalyst for rhodamine B degradation under visible light irradiation, Front Agric Sci Eng 4 (2017) 459–464, https://doi.org/10.15302/J-FASE-2017178.
[18] A. Piątkowska, M. Janus, K. Szymá Nski, S. Mozia, Catalysts review C-,N-and S-doped TiO 2 photocatalysts, A Review (2021), https://doi.org/10.3390/catal.
[19] W.P. Review, Rice production by country 2024, world population review. https://worldpopulationreview.com/country-rankings/rice-production-by-country%0A%0A, 2024. (Accessed 20 January 2024).
[20] J. Wakatuntu, P.W. Olupot, J. Jjagwe, E. Menya, M. Okure, Optimization of pyrolysis conditions for production of rice husk-based bio-oil as an energy carrier, Results in Engineering 17 (2023) 100947, https://doi.org/10.1016/j.rineng.2023.100947.
[21] A. Bazargan, Z. Wang, J.P. Barford, J. Saleem, G. McKay, Optimization of the removal of lignin and silica from rice husks with alkaline peroxide, J. Clean. Prod. 260 (2020), https://doi.org/10.1016/j.jclepro.2020.120848.
[22] A. Khan, V. Nair, J.C. Colmenares, R. Gläser, Lignin-based composite materials for photocatalysis and photovoltaics, Top. Curr. Chem. 376 (2018), https://doi.org/10.1007/s41061-018-0198-z.
[23] Q. Liu, S. Wang, Y. Zheng, Z. Luo, K. Cen, Mechanism study of wood lignin pyrolysis by using TG-FTIR analysis, J. Anal. Appl. Pyrolysis 82 (2008) 170–177, https://doi.org/10.1016/j.jaap.2008.03.007.
[24] E. Lizundia, M.H. Sipponen, L.G. Greca, M. Balakshin, B.L. Tardy, O.J. Rojas, D. Puglia, Multifunctional lignin-based nanocomposites and nanohybrids, Green Chem. 23 (2021) 6698–6760, https://doi.org/10.1039/d1gc01684a.
[25] R. Jia, C. He, Q. Li, S.Y. Liu, G. Liao, Renewable plant-derived lignin for electrochemical energy systems, Trends Biotechnol. 40 (2022) 1425–1438, https://doi.org/10.1016/j.tibtech.2022.07.017.
[26] J.C. De Haro, E. Tatsi, L. Fagiolari, M. Bonomo, C. Barolo, S. Turri, F. Bella, G. Griffini, Lignin-based polymer electrolyte membranes for sustainable aqueous dye-sensitized solar cells, ACS Sustain Chem Eng 9 (2021) 8550–8560, https://doi.org/10.1021/acssuschemeng.1c01882.
[27] J.L. Espinoza-Acosta, P.I. Torres-Chávez, J.L. Olmedo-Martínez, A. Vega-Rios, S. Flores-Gallardo, E.A. Zaragoza-Contreras, Lignin in storage and renewable energy applications: a review, J. Energy Chem. 27 (2018) 1422–1438, https://doi.org/10.1016/j.jechem.2018.02.015.
[28] B.K. Korir, J.K. Kibet, S.M. Ngari, A review on the current status of dye-sensitized solar cells: toward sustainable energy, Energy Sci. Eng. 12 (2024) 3188–3226, https://doi.org/10.1002/ese3.1815.
[29] M. Andrade-Guel, C. Cabello-Alvarado, C.A. Avila-Orta, M. Pérez-Alvarez, G. Cadenas-Pliego, P.Y. Reyes-Rodríguez, L. Rios-González, Green flame-retardant composites based on PP/TiO2/lignin obtained by melt-mixing extrusion, Polymers 14 (2022), https://doi.org/10.3390/polym14071300.
[30] Q. Abbas, S. Ilyas, M. Saleem, F. Alvi, R.U. Din, M. Shahzad, I. Sultana, A. Razaq, Fabrication and characterization of metal oxide and lignocelluloses fibers based working electrode for dye-sensitized solar cells (DSSCs), Mater. Res. Express 6 (2019), https://doi.org/10.1088/2053-1591/ab8cfa.
[31] M. Saleem, M. Irfan, S. Tabassum, M.D. Albaqami, M.S. Javed, S. Hussain, M. Pervaiz, I. Ahmad, A. Ahmad, M. Zuber, Experimental and theoretical study of highly porous lignocellulose assisted metal oxide photoelectrodes for dye-sensitized solar cells, Arab. J. Chem. 14 (2021), https://doi.org/10.1016/j.arabjc.2020.102937.
[32] E.S. Teixeira, V.F. Nunes, D.C. Pinho, P.H.F. Maia, F.M. Lima, M. de Sá Moreira, A.F.L. Almeida, F.N.A. Freire, Effect of the performance of lignin into the matrix of the TiO2 with application on DSSCs, Floresta e Ambiente 29 (2022), https://doi.org/10.1590/2179-8087-FLORAM-2022-0013.
[33] R. Varghese, S. Maria Jose, J. Thomas, Enhanced optical, electrical, dielectric, and photovoltaic properties in strontium titanate by Ce-doping through a modified combustion method, J. Integr. Sci. Technol 12 (4) (2024) 781, https://doi.org/10.62110/sciencein.jist.2024.v12.781.
[34] M.S. Rijal, M. Nasir, B.S. Purwasasmita, L.A.T.W. Asri, Cellulose nanocrystals-microfibrils biocomposite with improved membrane performance, Carbohydrate Polymer Technologies and Applications 5 (2023), https://doi.org/10.1016/j.carpta.2023.100326.
[35] C. Sriwong, K. Choojun, S. Sriwong, High photocatalytic performance of 3D porous-structured TiO2@natural rubber hybrid sheet on the removal of indigo carmine dye in water, SN Appl. Sci. 1 (2019), https://doi.org/10.1007/s42452-019-0900-y.
[36] J.S. Lupoi, S. Singh, R. Parthasarathi, B.A. Simmons, R.J. Henry, Recent innovations in analytical methods for the qualitative and quantitative assessment of lignin, Renew. Sustain. Energy Rev. 49 (2015) 871–906, https://doi.org/10.1016/j.rser.2015.04.091.
[37] N.C.D. Nath, J.C. Kim, K.P. Kim, S. Yim, J.J. Lee, Deprotonation of N3 adsorbed on TiO2 for high-performance dye-sensitized solar cells (DSSCs), J Mater Chem A Mater 1 (2013) 13439–13442, https://doi.org/10.1039/c3ta12298k.
[38] J. Guo, X. Chen, J. Wang, Y. He, H. Xie, Q. Zheng, The influence of compatibility on the structure and properties of PLA/lignin biocomposites by chemical modification, Polymers 12 (2020), https://doi.org/10.3390/polym12010056.
[39] R. Bhat, N. Abdullah, R.H. Din, G.S. Tay, Producing novel sago starch based food packaging films by incorporating lignin isolated from oil palm black liquor waste, J. Food Eng. 119 (2013) 707–713, https://doi.org/10.1016/j.jfoodeng.2013.06.043.
[40] Brebu M., Vasile C., Thermal degradation of lignin-A Review, Cellul. Chem. Technol. 44 (9) 353–363.
[41] V. Ramiah, Thermogravimetric and Differential Thermal Analysis of Cellulose, Hemicellulose, and Lignin, Applied polymer science, 1970.
[42] D.B. Tiz, F.A. Vicente, A. Kroflič, B. Likozar, Lignin-based covalent adaptable network Polymers—When bio-based thermosets meet recyclable by design, ACS Sustain Chem Eng 11 (2023) 13836–13867, https://doi.org/10.1021/acssuschemeng.3c03248.
[43] E. Galiwango, N.S.A. Rahman, A.H. Al-Marzouqi, M.M. Abu-Omar, A.A. Khaleel, Klason Method: an Effective Method for Isolation of Lignin Fractions from Date Palm Biomass Waste, Online, 2018. https://www.researchgate.net/publication/326983293.
[44] G. Lv, S. Wu, R. Lou, Hemicellulose pyrolysis, bioresource. https://www.researchgate.net/publication/233831909, 2010.
[45] H. Yang, R. Yan, H. Chen, C. Zheng, D.H. Lee, D.T. Liang, In-depth investigation of biomass pyrolysis based on three major components: hemicellulose, cellulose and lignin, Energy Fuel. 20 (2006) 388–393, https://doi.org/10.1021/ef0580117.
[46] S. Anand, A. Muthusamy, S. Dineshkumar, J. Chandrasekaran, Oxidative polycondensation of benzimidazole using NaOCl: synthesis, characterization, optical, thermal and electrical properties of polybenzimidazoles, J. Mol. Struct. 1147 (2017) 351–363, https://doi.org/10.1016/j.molstruc.2017.06.113.
[47] B. Lebeau, F. Jonas, P. Gaudin, M. Bonne, B. Lebeau, F. Jonas, P. Gaudin, M. Bonne, J.B.D. Depollution, Dyes Depollution of Water Using Porous TiO2-Based Photocatalysts to Cite This Version : HAL Id : Hal-03065639, 2020.
[48] O. Frank, M. Zukalova, B. Laskova, J. Kürti, J. Koltai, L. Kavan, Raman spectra of titanium dioxide (anatase, rutile) with identified oxygen isotopes (16, 17, 18), Phys. Chem. Chem. Phys. 14 (2012) 14567–14572, https://doi.org/10.1039/c2cp42763j.
[49] S.P. Zankowski, P.M. Vereecken, Electrochemical determination of porosity and surface area of thin films of interconnected nickel nanowires, J. Electrochem. Soc. 166 (2019) D227–D235, https://doi.org/10.1149/2.0311906jes.
[50] S.F. Shaikh, R.S. Mane, B.K. Min, Y.J. Hwang, O.S. Joo, D-sorbitol-induced phase control of TiO2 nanoparticles and its application for dye-sensitized solar cells, Sci. Rep. 6 (2016), https://doi.org/10.1038/srep20103.
[51] P. De, J. Halder, C.C. Gowda, S. Kansal, S. Priya, S. Anshu, A. Chowdhury, D. Mandal, S. Biswas, B.K. Dubey, A. Chandra, Role of porosity and diffusion coefficient in porous electrode used in supercapacitors – correlating theoretical and experimental studies, Electrochemical Science Advances 3 (2023), https://doi.org/10.1002/elsa.202100159.
[52] C. Lastoskie, K.E. Gubbins, N. Quirked, Pore size distribution analysis of microporous carbons: a density functional theory approach, J. Phys. Chem. 97 (1993) 4786–4796, https://doi.org/10.1021/j100120a035.

[53] L. Yu, W.L. Hsu, J.A. Shamim, H. Daiguji, Pore network modeling of a solid desiccant for dehumidification applications, Int J Heat Mass Transf 186 (2022), https://doi.org/10.1016/j.ijheatmasstransfer.2021.122456.
[54] K. Wang, Y. Zhuo, J. Chen, D. Gao, Y. Ren, C. Wang, Z. Qi, Crystalline phase regulation of anatase-rutile TiO2for the enhancement of photocatalytic activity, RSC Adv. 10 (2020) 43592–43598, https://doi.org/10.1039/d0ra09421h.
[55] K.H. Chung, B.J. Kim, Y.K. Park, S.C. Kim, S.C. Jung, Photocatalytic properties of amorphous n-doped tio2 photocatalyst under visible light irradiation, Catalysts 11 (2021), https://doi.org/10.3390/catal11081010.
[56] M.N.M. Ibrahim, A. Iqbal, C.C. Shen, S.A. Bhawani, F. Adam, Synthesis of lignin based composites of TiO2 for potential application as radical scavengers in sunscreen formulation, BMC Chem 13 (2019), https://doi.org/10.1186/s13065-019-0537-3.
[57] J. Liqiang, Q. Yichun, W. Baiqi, L. Shudan, J. Baojiang, Y. Libin, F. Wei, F. Honggang, S. Jiazhong, Review of photoluminescence performance of nano-sized semiconductor materials and its relationships with photocatalytic activity, Sol. Energy Mater. Sol. Cell. 90 (2006) 1773–1787, https://doi.org/10.1016/j.solmat.2005.11.007.
[58] R. Bhattacharjee, I. Hung, Effect of different concentration Li-doping on the morphology , defect and photovoltaic performance of Li – ZnO nanofibers in the dye-sensitized solar cells Effect of different concentration Li-doping on the morphology , defect and photovoltaic performanc, Mater. Chem. Phys. 143 (2019) 693–701, https://doi.org/10.1016/j.matchemphys.2013.09.055.
[59] D.M. Niedzwiedzki, Photophysical properties ofN719andZ907dyes, benchmark sensitizers for dye-sensitized solar cells, at room and low temperature, Phys. Chem. Chem. Phys. 23 (2021) 6182–6189, https://doi.org/10.1039/d0cp06629j.
[60] V.A. Online, H. Cheng, Y. Feng, Y. Fu, Y. Zheng, Y. Bai, Y. Shao, Mater. Chem. C (2022) 13590–13610, https://doi.org/10.1039/d2tc01869a.
[61] S. Ma, F. Liao, S. Li, M. Xu, J. Li, Effect of microstructure , grain size , and rare earth doping on the electrorheological performance of nanosized particle materials (2003) 3096–3102, https://doi.org/10.1039/b306996f.
[62] R. Bhattacharjee, I.M. Hung, Effect of different concentration Li-doping on the morphology, defect and photovoltaic performance of Li-ZnO nanofibers in the dye-sensitized solar cells, Mater. Chem. Phys. 143 (2014) 693–701, https://doi.org/10.1016/j.matchemphys.2013.09.055.
[63] M. Sakar, R. Mithun Prakash, D. Trong-On, Insights into the tio2-based photocatalytic systems and their mechanisms, Catalysts 9 (2019), https://doi.org/10.3390/catal9080680.
[64] J. Chae, D.Y. Kim, S. Kim, M. Kang, Photovoltaic efficiency on dye-sensitized solar cells (DSSC) assembled using Ga-incorporated TiO2 materials, J. Ind. Eng. Chem. 16 (2010) 906–911, https://doi.org/10.1016/j.jiec.2010.09.012.
[65] R. Krishnapriya, S. Praneetha, A.M. Rabel, A. Vadivel Murugan, Energy efficient, one-step microwave-solvothermal synthesis of a highly electro-catalytic thiospinel NiCo2S4/graphene nanohybrid as a novel sustainable counter electrode material for Pt-free dye-sensitized solar cells, J Mater Chem C Mater 5 (2017) 3146–3155, https://doi.org/10.1039/c6tc04619c.
[66] P. Wei, B. Hu, L. Zhou, T. Su, Y. Na, New strategy to incorporate nano-particle sized water oxidation catalyst into dye-sensitized photoelectrochemical cell for water splitting, J. Energy Chem. 25 (2016) 345–348, https://doi.org/10.1016/j.jechem.2016.03.020.
[67] N. Santhosh, K.B. Bhojanaa, P. Vijayakumar, M. Senthil Pandian, P. Ramasamy, A. Pandikumar, Electron migration between inter and intra particles in the soft-template processed titania nanospheres and its influences in the photovoltaic performance of the dye-sensitized solar cells, J. Mater. Sci. Mater. Electron. 31 (2020) 3910–3923, https://doi.org/10.1007/s10854-020-02936-4.
[68] C. Zhao, D. Child, Y. Hu, N. Robertson, D. Gibson, S.C. Wang, Y.Q. Fu, Low temperature growth of hybrid ZnO/TiO2 nano-sculptured foxtail-structures for dye-sensitized solar cells, RSC Adv. 4 (2014) 61153–61159, https://doi.org/10.1039/c4ra11881b.
[69] A.W. Morawski, E. Kusiak-Nejman, J. Przepiórski, R. Kordala, J. Pernak, Cellulose-TiO2 nanocomposite with enhanced UV-Vis light absorption, Cellulose 20 (2013) 1293–1300, https://doi.org/10.1007/s10570-013-9906-6.
[70] D. Guo, J. Zhang, L. Sha, B. Liu, X. Zhang, X. Zhang, G. Xue, Preparation and Preparation and characterization of lignin-TiO_2 UV-shielding composite material by induced synthesis with nanofibrillated cellulose, BioRes 15 (4) (2020) 7374–7389, https://doi.org/10.15376/biores.15.4.7374-7389.
[71] S. Yildirim, Synthesis, characterization and optical properties of Ag-doped TiO2 nanoparticles by flame spray pyrolysis, J. Mater. Sci. Mater. Electron. 32 (2021) 16346–16358, https://doi.org/10.1007/s10854-021-06187-9.
[72] S.A. Mozaffari, M. Ranjbar, E. Kouhestanian, H. Salar Amoli, M.H. Armanmehr, An investigation on the effect of electrodeposited nanostructured ZnO on the electron transfer process efficiency of TiO2 based DSSC, Mater. Sci. Semicond. Process. 40 (2015) 285–292, https://doi.org/10.1016/j.mssp.2015.06.081.
[73] Y. Yin, G. Huang, M. Di, C. Xue, W. Li, L. Zhang, Y. Liu, Increased electroactive species concentration in anodic biofilm of Geobacter-inoculated microbial fuel cells under static magnetic field, Res. Chem. Intermed. 43 (2017) 873–883, https://doi.org/10.1007/s11164-016-2670-0.
[74] Y. Lv, H. Zhang, C. Yang, W. Zhu, X. Zhou, Mesoporous sub-microsphere assembly of TiO2 nanocubes with highly exposed (101) facets and improved photovoltaic performance, J. Mater. Sci. Mater. Electron. 28 (2017) 16493–16503, https://doi.org/10.1007/s10854-017-7561-7.
[75] A.R. Agustin, K. Tamura, Surface modification of TiO2 nanoparticles with terephthalic acid in supercritical carbon dioxide, J. Supercrit. Fluids 174 (2021), https://doi.org/10.1016/j.supflu.2021.105245.
[76] M.N.M. Ibrahim, A. Iqbal, C.C. Shen, S.A. Bhawani, F. Adam, Synthesis of lignin based composites of TiO2 for potential application as radical scavengers in sunscreen formulation, BMC Chem 13 (2019) 1–14, https://doi.org/10.1186/s13065-019-0537-3.
[77] X. Chen, D.H. Kuo, D. Lu, Y. Hou, Y.R. Kuo, Synthesis and photocatalytic activity of mesoporous TiO2 nanoparticle using biological renewable resource of un-modified lignin as a template, Microporous Mesoporous Mater. 223 (2016) 145–151, https://doi.org/10.1016/j.micromeso.2015.11.005.
[78] P.R.F. Barnes, K. Miettunen, X. Li, A.Y. Anderson, T. Bessho, M. Gratzel, B.C. O'Regan, Interpretation of optoelectronic transient and charge extraction measurements in dye-sensitized solar cells, Adv. Mater. 25 (2013) 1881–1922, https://doi.org/10.1002/adma.201201372.
[79] E. Palomares, N.F. Montcada, M. Méndez, J. Jiménez-López, W. Yang, G. Boschloo, Photovoltage/photocurrent transient techniques, in: Characterization Techniques for Perovskite Solar Cell Materials, Elsevier, 2019, pp. 161–180, https://doi.org/10.1016/B978-0-12-814727-6.00007-4.
[80] Y. Firdaus, L.P. Maffei, F. Cruciani, M.A. Müller, S. Liu, S. Lopatin, N. Wehbe, G.O.N. Ndjawa, A. Amassian, F. Laquai, P.M. Beaujuge, Polymer Main-Chain Substitution Effects on the Efficiency of Nonfullerene BHJ Solar Cells 1700834 (2017) 1–11, https://doi.org/10.1002/aenm.201700834.